

## Article

# Adsorptive Removal of Sb(V) from Wastewater by Pseudo-Boehmite: Performance and Mechanism

Yating He, Qiming Mao \*, Yaoyu Zhou, Xiande Xie and Lin Luo \*

College of Environment and Ecology, Hunan Agricultural University, Changsha 410128, China; yatinghe0214@163.com (Y.H.); zhouyy@hunau.edu.cn (Y.Z.); xd\_xie@hunau.edu.cn (X.X.)

\* Correspondence: qimingmao@126.com (Q.M.); linluo@hunau.edu.cn (L.L.)

**Abstract:** With the increasing concern about antimony (Sb) pollution and remediation in aquatic ecosystems, more and more feasible technologies have been developed. Adsorption has been extensively studied due to the simplicity of its operation and its minimal environmental effects, but the lack of cheap and stable adsorbents has limited its application in Sb treatment. In this study, pseudo-boehmite (PB) was successfully synthesized via aluminum isopropylate hydrolysis, and its potential for removing Sb(V) from wastewater was explored. The removal efficiency of Sb(V) was 92.50%, and the maximum adsorption capacity was 75.25 mg/g under optimal conditions (pH 5.0, 2 g·L<sup>-1</sup> PB, and 10 mg·L<sup>-1</sup> Sb(V)). In addition, better performance could be obtained at acidic conditions (pH 3.0–5.0). Surface complexation, electrostatic attraction, and hydrogen bonding were identified as potential major processes for Sb(V) elimination by PB based on experimental and characterization data. This study presents a promising approach for the efficient removal of Sb(V) from wastewater, offering a new insight into the application of aluminum-based materials for heavy metal removal.

**Keywords:** antimony; pseudo-boehmite; adsorption; mechanism



**Citation:** He, Y.; Mao, Q.; Zhou, Y.; Xie, X.; Luo, L. Adsorptive Removal of Sb(V) from Wastewater by Pseudo-Boehmite: Performance and Mechanism. *Water* **2024**, *16*, 1172. <https://doi.org/10.3390/w16081172>

Academic Editor: Alexandre T. Paulino

Received: 18 March 2024

Revised: 8 April 2024

Accepted: 17 April 2024

Published: 20 April 2024



**Copyright:** © 2024 by the authors. Licensee MDPI, Basel, Switzerland. This article is an open access article distributed under the terms and conditions of the Creative Commons Attribution (CC BY) license (<https://creativecommons.org/licenses/by/4.0/>).

## 1. Introduction

Antimony (Sb) is a hazardous environmental contaminant, which has gained attention in recent years due to its potential carcinogenicity, uncontrolled mobility, and bioaccumulation [1]. Prolonged exposure to Sb can result in various health issues, including skin rashes, diarrhea, and chronic bronchitis [2]. More seriously, Sb could binds to specific enzymes in human cells, disrupting tissue metabolism and causing damage to the brain and reproductive system [2,3]. Mining and smelting of antimony ore have released large amounts of antimony into the environment [4]. The world's largest Sb mine is located in Hunan Province, China, and the Sb content in the water around the mine area could reach 224~6384 µg·L<sup>-1</sup> [4,5]. Considering the potential environmental risks of Sb, the maximum contamination level of Sb in drinking water in China is 5 µg·L<sup>-1</sup>, which is more strict than the standards of the World Health Organization (20 µg·L<sup>-1</sup>) and the US Environmental Protection Agency (6 µg·L<sup>-1</sup>) [6].

Sb usually exists in four valence states: Sb(-III), Sb(0), Sb(III) and Sb(V). Sb(III) and Sb(V) are the two major types in aquatic environments, with Sb(V) being the most stable oxidation state and the primary form in the natural environment [7]. Since the toxicity of Sb(III) compounds is ten times higher than that of Sb(V) compounds, the removal of Sb(III) has received more attention in research studies. However, Sb(V) generally exhibits higher mobility and solubility than Sb(III), making it more challenging to handle due to its stability [8]. The primary form of Sb(V) is [Sb(OH)<sub>6</sub>]<sup>-1</sup>, which is the most stable form in oxygen-containing aqueous systems over a broad pH range of 2.0 to 14.0 [9]. Therefore, it is equally important to explore effective methods for the removal of Sb(V) from the aqueous environment.

A variety of methods have been used to remove Sb from contaminated water, such as adsorption [10], chemical precipitation [11], membrane filtration [12], flocculation [13], and

ion exchange [14]. Among them, adsorption methods have gained widespread attention due to their simplicity in operation, minimal environmental impact, high removal efficiency, and the potential for recycling the consumed adsorbents. In recent years, various adsorbent materials, especially nanostructured metal oxides/hydroxides, have been developed for the removal of antimony from aqueous solutions [6,15,16]. Iron-based nanoparticles such as  $\text{Fe}_2\text{O}_3$ ,  $\text{Fe}_3\text{O}_4$ , nano zero-valent iron (nZVI), and  $\text{FeOOH}$  are among the most often utilized adsorbent materials. Despite the excellent adsorption performance exhibited by these iron-based materials, their smaller surface area, lower  $\text{pH}_{\text{pzc}}$ , and chemical instability within the pH range of interest limit their effective utilization in antimony remediation processes [17]. Furthermore, the high production cost of iron-based nanoparticles materials makes them unsuitable for large-scale promotion or application in practical production.

Aluminum-based materials have attracted extensive attention in the treatment of antimony-contaminated water due to their high isoelectric point, large specific surface area, chemical stability, and non-toxicity [18]. For instance, Sai et al. investigated the DFT of Sb(V) oxyanion adsorption on  $\alpha\text{-Al}_2\text{O}_3$ ; their results indicated that Sb(V) tends to adopt bidentate and tridentate geometries on the surface, with Sb binding through the corners of  $\text{AlO}_6$  groups [19]. Zhou et al. found that the adsorption of Sb(V) on  $\gamma\text{-Al}_2\text{O}_3$  is in the form of outer-sphere complexes [20]. Boehmite ( $\gamma\text{-AlOOH}$ ) has been extensively utilized to remove different anionic contaminants as common representative aluminum phases [21,22]. The weakly crystalline phase of boehmite, known as pseudo-boehmite (PB), has a porous structure, high positive surface charge, greater specific surface area ( $224\text{--}445\text{ m}^2\cdot\text{g}^{-1}$ ) and abundant surface hydroxyl groups [22–24]. These unique properties make it beneficial for the removal of Sb(V) oxyanions. Furthermore, its layered structure enables controlled release of adsorbed substances under specific conditions, making it highly advantageous for applications involving adsorption–desorption cycles. These features imbue it with significant potential for widespread applications in the field of water treatment. However, PB has never been used for Sb(V) removal, and the adsorption mechanism of PB on antimony is not clear. We will therefore further investigate the feasibility of PB, along with its adsorption behavior and removal mechanisms.

In this study, we prepared PB via aluminum isopropylate hydrolysis and systematically characterized its morphological and chemical properties. The aim was to evaluate the adsorption performance of aqueous solutions on Sb(V) under various conditions (PB dosage, Sb(V) concentration, pH, presence of coexisting common metal cation, anions and humic). Furthermore, on the basis of experimental results and characterization analysis, the removal mechanism of Sb(V) by PB was discussed. Adsorption–regeneration experiments were used to evaluate the reusability of PB. This study provides new insights into the removal of Sb from wastewater using aluminum-based materials.

## 2. Materials and Methods

### 2.1. Chemicals and Reagents

In this study, every chemical and reagent used was analytical grade or above, and could be used directly without the need for additional purification. Unless otherwise stated in this study, all solutions were prepared using deionized water (DW). Aluminum isopropoxide, isopropyl alcohol and potassium pyroantimonate ( $\text{KSbO}_6\text{H}_6$ , AR) were obtained from Macklin Biochemical Technology Co., Ltd. (Shanghai, China). Other reagents such as hydrochloric acid (HCl), sodium hydroxide (NaOH), nitric acid ( $\text{HNO}_3$ ), etc. were purchased from Sinopharm Chemical Reagent. (Shanghai China). A stock solution containing  $1000\text{ mg}\cdot\text{L}^{-1}$  of Sb(V) was made and then diluted to the necessary concentration for future usage.

### 2.2. Preparation of PB

PB was prepared via aluminum isopropylate hydrolysis. Then, 50 g aluminium isopropoxide and 30 mL isopropanol were placed in a 250 mL three-mouth flask and dissolved into a transparent light yellow liquid at 120 rpm,  $55\text{ }^\circ\text{C}$ . Afterward, 30 mL DW

was added to the mixture and continually stirred for 3 h. Finally, the product was washed with DW until the pH reached 6.0, dried at 80 °C for 10 h, and then ground through a 100 mesh with an agate mortar for further adsorption experiments.

### 2.3. Characterization of PB

The surface morphology of the synthesized PB was analyzed using scanning electron microscopy (Zeiss supra55, Carl Zeiss, Germany). The surface functional groups of PB were characterized utilizing Fourier transform infrared spectroscopy (FTIR) (Nicolet 5077, Thermo Fisher, USA). The porous structure and the specific surface area of PB were analyzed using a low-temperature nitrogen adsorption/desorption isotherm (Gemini-2390, Micromeritics CORP, USA). Using the Nano S90 Zetasizer Zeta potential instrument (Malvern Panalytical, Malvern, UK), the isoelectric point ( $\text{pH}_{\text{pzc}}$ ) of PB was determined. The Zeta potential of PB was determined under the conditions of a solution pH ranging from 5.0 to 11.0 and a mass fraction of 0.1%. The AXIS SUPRA X-ray photoelectron spectroscopy (XPS) instrument from Shimadzu Corporation, Japan, was utilized for the analysis of PB, and data were fitted using Thermo Avantage (v5.99) software.

### 2.4. Adsorption Experiments

#### 2.4.1. Effect of Solution pH

A certain amount of adsorbent and 100 mL of a known concentration Sb(V) solution were added into 250 mL conical flasks and placed in a vibrational reactor operating at 150 rpm. The oscillation lasted for 30 min under the condition of 298 K. Subsequently, the supernatant was filtered through a 0.45  $\mu\text{m}$  filter membrane. The primary focus of the study on variations in dosages was to identify the optimal dosage of materials required for batch experiments. The dosage study confirmed that an adsorbent dose of 2  $\text{g}\cdot\text{L}^{-1}$  was used for all batch trials (Figure S1). The pH variation study was conducted by adjusting the pH of a 10  $\text{mg}\cdot\text{L}^{-1}$  Sb(V) solution within the range of 3.0 to 10.0.

#### 2.4.2. Kinetic and Isotherms Adsorption Experiments

Kinetic adsorption experiments were performed by adding 0.2 g PB into 100 mL of 10  $\text{mg}\cdot\text{L}^{-1}$  Sb(V) solution at  $\text{pH} = 5.0 \pm 0.2$  and shaking (150 rpm) at 298 K for 30 min. Adsorption isotherm experiments were conducted by adding 0.2 g PB to 100 mL Sb(V) solution with varying concentrations (10–300  $\text{mg}\cdot\text{L}^{-1}$ ) at  $\text{pH} = 5.0 \pm 0.2$  and then shaking at 150 rpm for 30 min at 298 K, 308 K, and 318 K. The supernatant of the sample was collected at different time intervals for analysis with an inductively coupled plasma emission spectrometer (ICP-OES). All batch adsorption experiments were repeated three times, and the average of the experimental results was taken as the valid data. SPSS Statistics29 was used for data processing, and OriginPro 2021b was employed to fit the data regression line. Additionally, the equations were presented in the form shown in Tables 1 and 2.

**Table 1.** Kinetics equations for adsorption of Sb(V) on PB.

Kinetics Type	Equations	Description of Parameters
Pseudo-first-order kinetics	$\ln(q_e - q_t) = \ln q_e - \frac{k_1}{2.303} t$	$k_1$ ( $\text{mg}\cdot\text{L}^{-1}$ ), adsorption rate constant; $q_e$ ( $\text{mg}\cdot\text{g}^{-1}$ ) and $q_t$ ( $\text{mg}\cdot\text{g}^{-1}$ ), sorption capacities at equilibrium and at any time.
Pseudo-second-order kinetics	$\frac{t}{q_t} = \frac{1}{k_2 q_e^2} + \frac{t}{q_t}$	$k_2$ ( $\text{g}\cdot\text{mg}^{-1}\cdot\text{min}^{-1}$ ), adsorption rate constant; $q_e$ ( $\text{mg}\cdot\text{g}^{-1}$ ) and $q_t$ ( $\text{mg}\cdot\text{g}^{-1}$ ), sorption capacities at equilibrium and at any time.
Elovich model	$q_t = \frac{1}{\beta} \ln \alpha \beta + \frac{1}{\beta} \ln t$	$q_t$ ( $\text{mg}\cdot\text{g}^{-1}$ ), sorption capacity at any time; $\alpha$ ( $\text{mg}\cdot\text{mL}^{-1}\cdot\text{min}^{-1}$ ) and $\beta$ ( $\text{mL}\cdot\text{mg}^{-1}$ ), the initial adsorption coefficient and Elovich model equation constants.
Intraparticle diffusion model	$q_t = k_3 t^{1/2} + C$	$k_3$ ( $\text{mg}\cdot\text{g}^{-1}\cdot\text{min}^{-1/2}$ ), adsorption rate constant; $q_t$ ( $\text{mg}\cdot\text{g}^{-1}$ ) sorption capacity at any time; C is a constant.

**Table 2.** Isotherm equations for adsorption of Sb(V) on PB.

Models	Equations	Description of Parameters
Langmuir	$q_e = \frac{Q_{max}K_L C_e}{1 + K_L C_e}$	$K_L$ ( $L \cdot mg^{-1}$ ), adsorption equilibrium constant; $q_e$ ( $mg \cdot g^{-1}$ ) and $C_e$ ( $mg \cdot L^{-1}$ ), equilibrium sorption capacity of adsorbent and equilibrium concentration of adsorbate, respectively. $Q_{max}$ is calculated saturated adsorption capacity.
Freundlich	$q_e = K_F C_e^{1/n}$	$K_F$ ( $L \cdot mg^{-1}$ ) and $n$ , adsorption equilibrium constant, characteristic constant characterizing the properties of adsorption force, respectively; $q_e$ ( $mg \cdot g^{-1}$ ) and $C_e$ ( $mg \cdot L^{-1}$ ), equilibrium sorption capacity of adsorbent and equilibrium concentration of adsorbate, respectively.
Temkin	$q_e = \frac{RT}{b_T} \ln k_T + \frac{RT}{b_T} \ln C_e$	$R$ , universal gas constant ( $8.314 J \cdot mol^{-1} \cdot K^{-1}$ ); $k_T$ ( $L \cdot mg^{-1}$ ) and $b_T$ , equilibrium binding constant and Temkin isotherm constant, respectively; $q_e$ ( $mg \cdot g^{-1}$ ) and $C_e$ ( $mg \cdot L^{-1}$ ), equilibrium sorption capacity of adsorbent and equilibrium concentration of adsorbate, respectively.
Dubinin–Radushkevich	$\ln q_e = \ln q_m - \beta \xi^2$ $\xi = RT \ln \left( 1 + \frac{1}{C_e} \right)$	$\beta$ ( $mol^2 \cdot kJ^{-2}$ ) and $\xi$ , Dubinin–Radushkevich isotherm constants; $T$ and $R$ , absolute temperature (K) and universal gas constant ( $8.314 J \cdot mol^{-1} \cdot K^{-1}$ ), respectively; $C_e$ ( $mg \cdot L^{-1}$ ), equilibrium concentration of adsorbate. $q_e$ ( $mg \cdot g^{-1}$ ) and $q_m$ ( $mg \cdot g^{-1}$ ), equilibrium sorption capacity of adsorbent and theoretical isotherm saturation capacity, respectively.

#### 2.4.3. The Coexistence Effect of Common Metal Cation and Anions and Humic Acid

The influence of ionic strength on the adsorption of Sb(V) was assessed at a concentration of  $10 \text{ mg} \cdot \text{L}^{-1}$  Sb(V), pH  $5.0 \pm 0.2$  and rotational speed of 150 rpm. The effect of common metal cations and anions and humic acid on Sb(V) adsorption were evaluated by adding 5.0 mM, 10.0 mM, and 20.0 mM of corresponding chlorine salts (NaCl, CaCl<sub>2</sub>, MgCl<sub>2</sub>, KCl and AlCl<sub>3</sub>), sodium slats (NaCl, Na<sub>2</sub>SO<sub>4</sub>, Na<sub>2</sub>HPO<sub>4</sub>, Na<sub>2</sub>SiO<sub>3</sub>, Na<sub>2</sub>CO<sub>3</sub> and NaNO<sub>3</sub>), and humic acid ( $1\text{--}50 \text{ mg} \cdot \text{L}^{-1}$ ), respectively.

#### 2.5. The Adsorbent Regeneration

Briefly, 0.2 g PB was added to 100 mL of  $10 \text{ mg} \cdot \text{L}^{-1}$  Sb(V) solution in the same procedure as the adsorption experiment. After sorption, PB was collected by centrifugation at 8000 rpm for 15 min using 100 mL centrifuge tubes, and the precipitate was dried with a freeze dryer for 48 h. Then, 30 mL DW or  $1.0 \times 10^{-4} \text{ M}$  NaOH (pH = 10.0) was added as desorbing agents, and the suspension was oscillated at 150 rpm for 2 h to desorb Sb(V) from PB. The adsorbent was rinsed with distilled water until the pH reached 6.0 then added to 100 mL of  $10 \text{ mg} \cdot \text{L}^{-1}$  Sb(V) solution. The above adsorption–desorption process was repeated 4–5 times.

### 3. Results and Discussion

#### 3.1. Characterization of Materials

The surface morphology of adsorbent is depicted in (Figure 1a–c). PB showed a large pore distribution formed by particle accumulation with a more loose and porous structure. The PB particles obtained by the hydrolysis of aluminum isopropanol had a complete crystal structure, spherical shape and uniform spacing, and the spherical particles agglomerated to form PB. In addition, the surface of these spherical particles was rough (Figure 1c), which was beneficial to the adsorption of Sb(V) [25]. The XRD patterns of PB are illustrated in Figure 1d. The peaks of the prepared adsorbent at  $13.9^\circ$ ,  $28.3^\circ$ ,  $38.5^\circ$ ,  $49.2^\circ$ , and  $64.8^\circ$  positions were well matched with the characteristic peaks of PB [26]. The FTIR spectra of the PB are presented in Figure 1e. The peaks that occurred at  $3422 \text{ cm}^{-1}$ ,  $2093 \text{ cm}^{-1}$ , and  $1396 \text{ cm}^{-1}$  could be attributed to the tensile vibrational overlap of the O–H bonds [27,28]. Moreover, the peak obtained at  $1072 \text{ cm}^{-1}$  was due to the symmetric bending vibration of the Al–O–H bond [29,30], and the peak at  $1632 \text{ cm}^{-1}$  corresponded to the stretching and bending vibration of the surface H–O–H bond [26]. In addition, the vibrational band obtained at  $499 \text{ cm}^{-1}$  was the characteristic peak of the Al–O bond present in the AlO<sub>6</sub>

octahedral lattice of PB. The specific surface area and variety of porosity of the synthesized adsorbents were analyzed using the  $N_2$  adsorption–desorption isotherm. As shown in Figure 1f, the calculated specific surface area of PB was  $307.9 \text{ m}^2 \cdot \text{g}^{-1}$ , and the resulting BET curve exhibited traits of the H3 hysteresis loop and a type IV isotherm, indicating that the synthesized material has meso-porous properties and good pore connectivity with channel-like or ink-bottle pores [31]. Higher closure points in loops above  $P/P_0 = 0.9$  might indicate the existence of bigger pores and a wider variety of pore sizes [32], and the high surface area and porous structure of the adsorbent implied the availability of more adsorption sites. Based on the desorption data from the BJH pore size distribution, the calculated average pore diameter of the material was 6.71 nm, with a pore volume of  $0.564 \text{ cm}^3 \cdot \text{g}^{-1}$ . These data supported the mesoporous characteristics of the prepared adsorbent material.

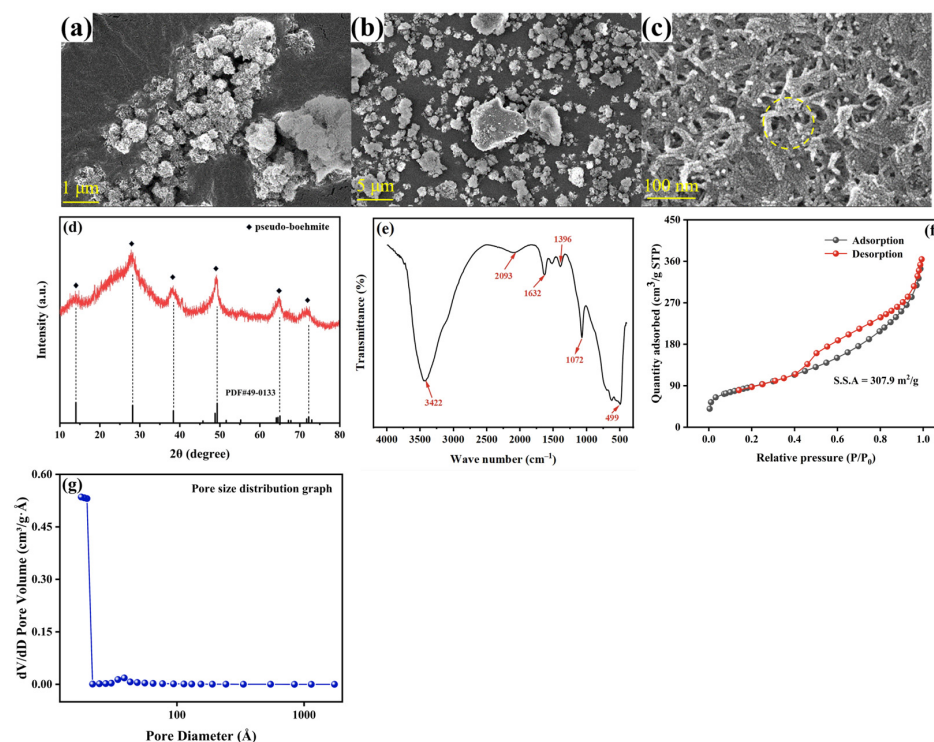


**Figure 1.** (a–c) SEM micrographs of the prepared PB (left to right: lower to higher magnifications), (d) X-ray diffraction patterns of the PB, (e) FTIR spectra of PB, (f)  $N_2$  adsorption–desorption isotherm of PB. The inset of (g) shows the pore size distribution graph of the material.

### 3.2. Adsorption Kinetics

Kinetic models can characterize the adsorption rate, unveil the chemical and physical properties of PB, and serve as a key factor in assessing adsorption efficiency and optimizing adsorbent operational conditions. Figure 2 displayed the outcome of the investigation into the time-dependent adsorption behavior of Sb(V) by PB. As shown in Figure 2a,b, the rapid adsorption of Sb(V) on PB occurred within the initial 2 min, followed by a slow phase until reaching adsorption equilibrium, demonstrating a faster adsorption rate compared to other adsorbents [33–36]. On the one hand, the initial high specific surface area of PB facilitates rapid occupation of empty surface attachment sites by pollutants, leading to their physical adsorption upon proximity to the adsorbent. On the other hand, the existence of active and oxygen-containing functional groups on the PB surface enabled an ion exchange reaction with Sb(V), resulting in complex formation and subsequent removal through chemisorption. Furthermore, during the adsorption process of Sb(V) by PB, there was no leaching of aluminum ions (Figure S2). However, iron-based nanoparticles such as nZVI were lost when Sb was adsorbed [15], which indicated the excellent stability of PB.

The equation is presented in the form shown in Table 1, and fitting results are listed in Table 3. It is clear that the  $R^2$  (0.999) of the pseudo-second-order kinetics was much greater than  $R^2$  (0.779) of the pseudo-first-order kinetics, implying that chemical adsorption might be the primary adsorption mechanism [37]. In addition, the  $q_e$  value calculated by the pseudo-second-order kinetics was more compatible with the experimental  $q_e$  value, which once again proved that the pseudo-second-order kinetics was more appropriate for the removal process of Sb(V). The Elovich model (Figure 2c) could also better fit the adsorption of PB on Sb(V), suggesting that the adsorption process was controlled by both reaction rate and diffusion [38].

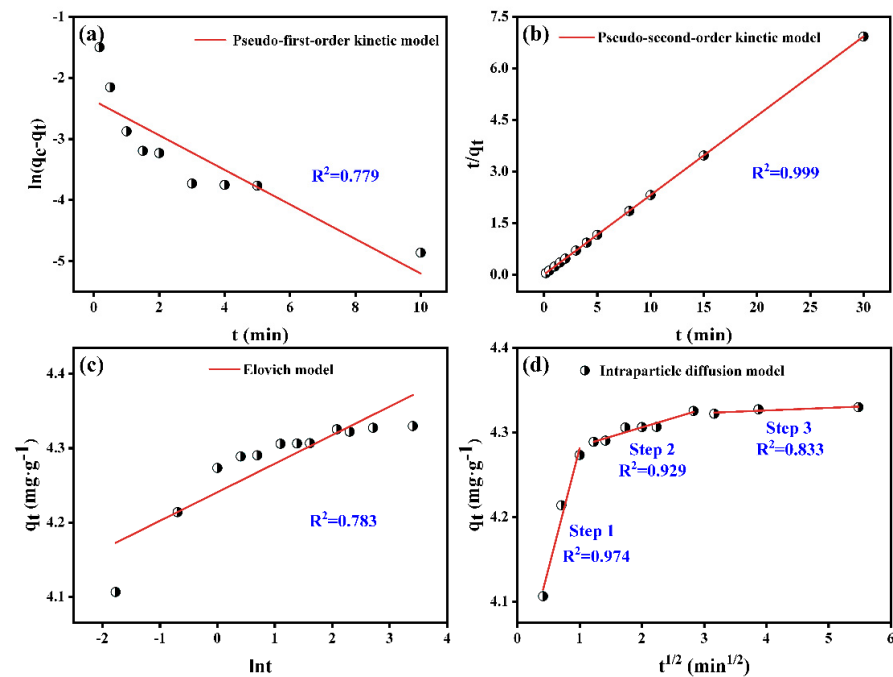


**Figure 2.** Adsorption kinetics for Sb(V) adsorption on PB: (a) Pseudo-first-order kinetic model, (b) Pseudo-second-order kinetic model, (c) Elovich model, (d) intraparticle diffusion model. Reactive time, 0–30 min; temperature of 298 K;  $\text{pH}_{\text{initial}} = 5.0$ ; adsorbent dosage,  $2 \text{ g}\cdot\text{L}^{-1}$ .

**Table 3.** Kinetics adsorption parameters of Sb(V) on PB.

Adsorption Kinetics Models	Parameters	Sb(V)
Pseudo-first-order kinetic model	$k_1$ ( $\text{min}^{-1}$ )	0.651
	$q_{e1}$ ( $\text{mg}\cdot\text{g}^{-1}$ )	0.093
	$R^2_1$	0.779
Pseudo-second-order kinetic model	$k_2$ ( $\text{g}\cdot\text{mg}^{-1}\cdot\text{min}^{-1}$ )	13.793
	$q_{e2}$ ( $\text{mg}\cdot\text{g}^{-1}$ )	4.328
	$q_{e \text{ experiment}}$ ( $\text{mg}\cdot\text{g}^{-1}$ )	4.333
	$R^2_2$	0.999
Elovich model	$\alpha$ ( $\text{mg}\cdot\text{mL}^{-1}\cdot\text{min}^{-1}$ )	0.297
	$\beta$ ( $\text{mL}\cdot\text{mg}^{-1}$ )	26.001
	$R^2$	0.783
Intraparticle diffusion model	$K_{d1}$ ( $\text{mg}\cdot\text{g}^{-1}\cdot\text{min}^{-1/2}$ )	0.284
	$C_1$	3.997
	$R^2_1$	0.974
	$K_{d2}$ ( $\text{mg}\cdot\text{g}^{-1}\cdot\text{min}^{-1/2}$ )	0.022
	$C_2$	4.262
	$R^2_2$	0.929
	$K_{d3}$ ( $\text{mg}\cdot\text{g}^{-1}\cdot\text{min}^{-1/2}$ )	0.003
	$C_3$	4.314
	$R^2_3$	0.833

To investigate the Sb(V) diffusion mechanism from solution to PB in more detail, the intraparticle diffusion model was fitted and analyzed on the obtained experimental data. The fitting results are presented in Figure 2d and Table 3. The adsorption correlation coefficients ( $R^2$ ) were all between 0.833 and 0.974, which implied that the intra-particle diffusion model could well simulate the adsorption process of PB on Sb(V) in each corresponding adsorption stage. In the first step, after the rapid occupation of excellent active adsorption sites on the surface of PB by Sb(V), an external surface adsorption or instantaneous adsorption appeared. With the increase in adsorption positions occupied by Sb(V), the adsorption in the second stage slowed down gradually, diffusion adsorption into internal pores occurred in the next adsorption step, and the adsorption equilibrium stage was the final phase. It could be concluded that there were other limiting steps outside the pore diffusion process since the linear fitting of each stage did not go through the origin [32].

### 3.3. Adsorption Isotherms

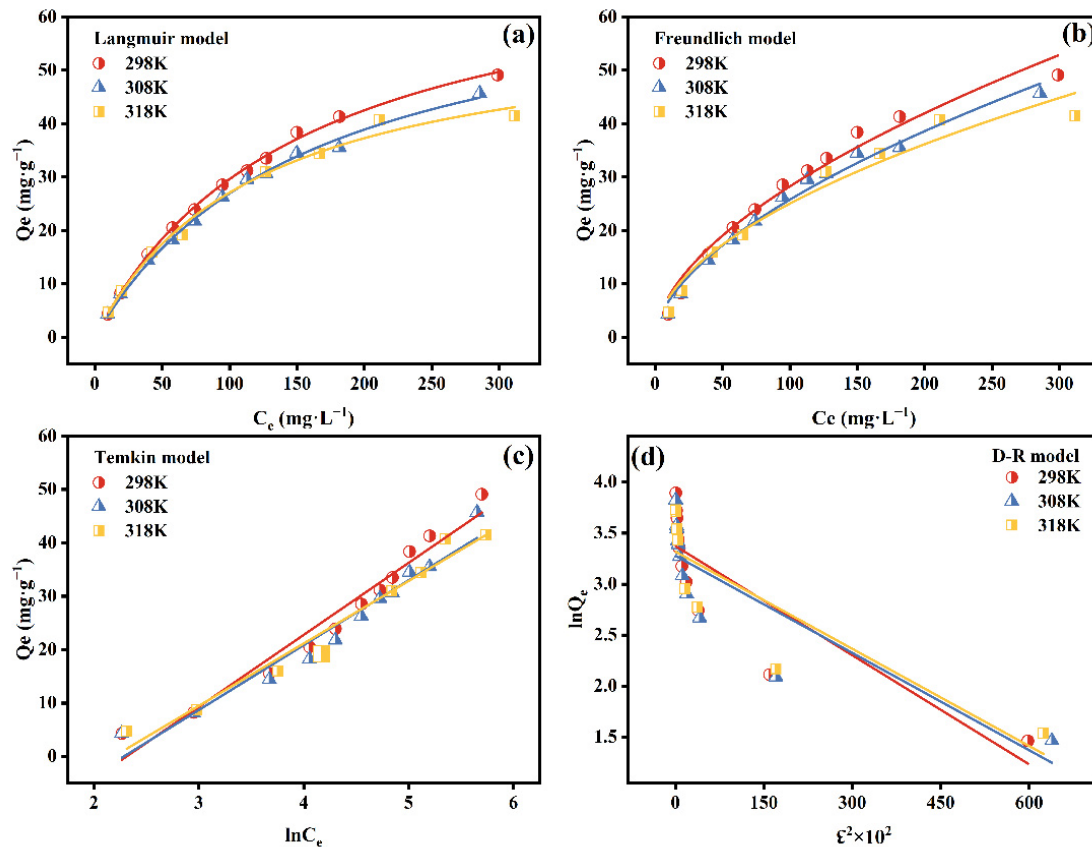
Isothermal simulation is of great significance for determining the type of adsorbent and determining its capacity. The Langmuir model posits that single-molecule adsorption takes place on a homogeneous surface primarily through ion exchange. Once an adsorbent occupies a specific position on the adsorbent surface, no further adsorption occurs at that site. In contrast, the Freundlich model assumes multi-layer adsorption processes on heterogeneous surfaces, primarily dominated by complexation [39]. The equations forms are in Table 2. The fitted results are shown in Figure 3a–d and Table 4. The Langmuir model demonstrated a higher  $R^2$  value (0.99) compared to other models, indicating that Sb(V) removal was primarily dominated by monolayer homogeneous chemisorption [5,37]. At pH 5.0 and 298 K, the calculated  $Q_{max}$  of PB was  $75.25 \text{ mg}\cdot\text{g}^{-1}$ . The Freundlich model exhibited a good fit ( $R^2 = 0.965\text{--}0.985$ ), revealing that heterogeneous multilayer chemical adsorption was connected with the adsorption process. Furthermore, the Freundlich indices ( $n^{-1}$ ) were 0.57 (298 K), 0.58 (308 K) and 0.53 (318 K), all of which were between 0 and 1, which indicated that the adsorption process occurred easily. Table 4 demonstrated that the  $R^2$  for the Temkin model was greater than 0.94, indicating that the adsorption process might be influenced by the interaction between the adsorbent and the adsorbate [40]. The D-R model is typically used to explain how adsorbent fills pores, and its fitting value was  $R^2 < 0.760$ . The low  $R^2$  value indicated that the adsorption process was not a simply physical adsorption, which was consistent with the results obtained from the kinetic fitting. Additionally, the adsorption capacity of PB was compared with those of several other materials, as shown in Table 5, clarifying that PB is one of the adsorbents with relatively better Sb(V) removal.

**Table 4.** Linear correlation analysis and parameter values of adsorption isothermal models.

Isothermal Models	Parameters	Temperature (K)		
		298 K	308 K	318 K
Langmuir model	$k_L$ ( $\text{L}\cdot\text{mg}^{-1}$ )	0.007	0.006	0.008
	$q_{max}$ ( $\text{mg}\cdot\text{g}^{-1}$ )	75.25	69.92	59.77
	$R^2$	0.998	0.996	0.991
Freundlich model	$k_f$ ( $\text{L}\cdot\text{mg}^{-1}$ )	2.05	1.77	2.18
	$n^{-1}$	0.57	0.58	0.53
	$R^2$	0.976	0.985	0.965
Temkin model	$k_T$ ( $\text{L}\cdot\text{mg}^{-1}$ )	13.48	12.14	11.68
	$b_T$	183.80	210.93	226.36
	$R^2$	0.956	0.949	0.963
D-R model	$q_m$ ( $\text{mg}\cdot\text{g}^{-1}$ )	29.18	26.56	27.64
	$\beta$ ( $\text{mol}^2\cdot\text{kJ}^{-2}$ )	0.004	0.003	0.003
	$R^2$	0.746	0.736	0.755

**Table 5.** Comparison of reported adsorption capacities for Sb(V).

Adsorbents	pH	$q_e$ (mg·g <sup>-1</sup> )	Reference
Fe–Zr amorphous oxides	7.0 ± 0.2	51	[41]
Fe(OH) <sub>3</sub>	4	24.47 ± 2.79	[34]
Ce-doped magnetic biochar	7.5	25.0	[35]
Nano zirconium iron oxide based on activated carbon	5.0	11.8	[36]
TiO <sub>2</sub> particles	2.2 ± 0.1	12.0	[16]
PB	5.0	75.25	this work

**Figure 3.** The adsorption isotherm fitted plots of Langmuir model (a), Freundlich model (b), Temkin model (c) and D-R model (d) for the adsorption of Sb(V) on PB at different temperatures. Reactive time, 0–30 min; temperature of 298 K; pH<sub>initial</sub> = 5.0; adsorbent dosage, 2 g·L<sup>-1</sup>.

### 3.4. Effect of pH

Since the pH of the solution affects both the adsorbent's surface charge and the chemical state of antimony, it is crucial to assess the antimony removal efficiency of the material under different pH conditions. The experimental results of the pH variation research and the zeta potential of PB are displayed in Figures 4a and 4b, respectively. The data showed that the isoelectric point appeared at 9.4; generally, a higher pH<sub>pzc</sub> is thought to indicate that the material's surface has a rich positive charge and has a good affinity for antimony anions. Within the pH range of 3.0–5.0, the removal efficiency of Sb(V) by the adsorbent material was 90.32–99.10%. With the increase in pH, the removal rate of Sb(V) from PB continued to decrease. At pH<sub>initial</sub> = 10.0, the adsorption rate of Sb(V) decreased to 54.89%. At pH<sub>initial</sub> < 9.4, the surface of PB protons containing H<sup>+</sup> was positively charged, which was beneficial for electrostatic attraction with [Sb(OH)<sub>6</sub>]<sup>-</sup>. At pH<sub>initial</sub> < 9.4, Sb(V) was still adsorbed by negatively charged PB. This might be attributed to chemical interactions between PB and Sb(V), such as ion exchange. When pH<sub>initial</sub> < 7.0, the final pH value of Sb(V) adsorbed by PB increased, indicating that PB participated in the

ligand exchange reaction under acidic conditions, replacing  $-OH$  in solution and releasing hydroxide ions. When the  $pH_{initial} > 7.0$ , the final pH was lower than the initial pH. This could be ascribed to the formation of the Al-O-Sb complexes, which would release  $H^+$  during the interaction. Since the amount of  $OH^-$  and  $H^+$  released or neutralized in the solution was small, the equilibrium pH tended to be the initial value at  $pH_{initial} = 7.0$ . A similar trend was observed in other adsorbents [9].

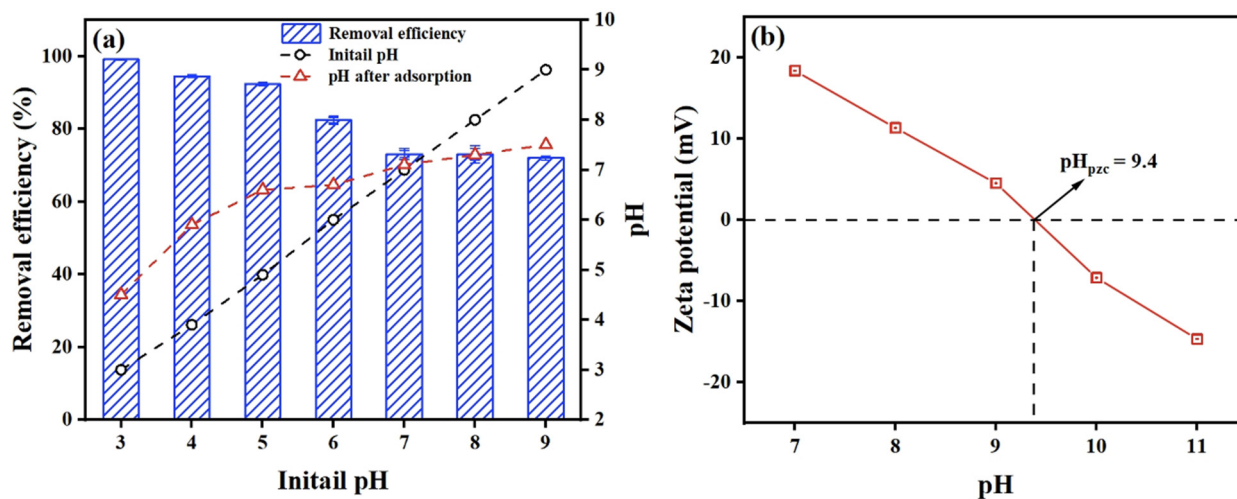


**Figure 4.** (a) Effect of pH on equilibrium adsorption Sb(V) by PB (experimental conditions:  $[Sb(V)]_0 = 10 \text{ mg}\cdot\text{L}^{-1}$ ; adsorbent dosage,  $2 \text{ g}\cdot\text{L}^{-1}$ ; temperature of 298 K; reactive time, 0–30 mi); (b) Zeta potential of the PB as a function of solution pH.

### 3.5. Interference of Co-Existing Ions and Humic Acid

The complex system of the natural environment, inorganic ions, and organics commonly found in aqueous solution may interfere with the adsorption of Sb(V) on the PB surface by competing for effective binding sites. The impact of cations ( $Na^+$ ,  $Ca^{2+}$ ,  $Mg^{2+}$ ,  $K^+$  and  $Al^{3+}$ ), anions ( $Cl^-$ ,  $SiO_3^{2-}$ ,  $CO_3^{2-}$ ,  $HPO_4^{2-}$ ,  $NO_3^-$  and  $SO_4^{2-}$ ), and humic acid on the adsorption of Sb(V) by PB was therefore investigated. As shown in Figure 5a–c, even as the concentration of  $SiO_3^{2-}$  continued to increase, the effect on the Sb(V) removal process remained negligible. Moreover, the effect of  $CO_3^{2-}$  and  $NO_3^-$  on the adsorption of Sb(V) by PB was minimal. The presence of  $HPO_4^{2-}$  and  $SO_4^{2-}$  significantly reduced the Sb(V) removal efficiency, with 16.92% and 35.39% retained, respectively. Phosphate and Sb are widely thought to be placed in the VA group, which exhibit the same physicochemical properties as Sb under acidic conditions. It exhibited substantial competitive interference behavior when Sb(V) was removed because it could form an inner-sphere complex with adsorption sites [9,37]. In addition, different concentrations of  $Na^+$  also had a subtle effect on the adsorption of Sb(V), but there was no difference in the degree and law of inhibition of  $Ca^{2+}$ ,  $Mg^{2+}$  and  $K^+$ . The presence of  $Al^{3+}$  had a significant impact on the adsorption of Sb(V). As the concentration of  $Al^{3+}$  increased to 20.0 mM, the removal efficiency of Sb(V) by PB reduced to 56.53%. This could be explained by the hydrolysis of  $Al^{3+}$  in acidic solutions, which inhibited the activity of adsorption sites on the surface of PB, resulting in lower removal efficiency. Furthermore, the influence of humic acid on the adsorption of Sb(V) should not be overlooked. At concentrations of  $10 \text{ mg}\cdot\text{L}^{-1}$  or more, humic acid had a significant interfering effect on Sb(V) removal, which can be explained as the ability of humic acid macromolecules to inhibit surface active sites.

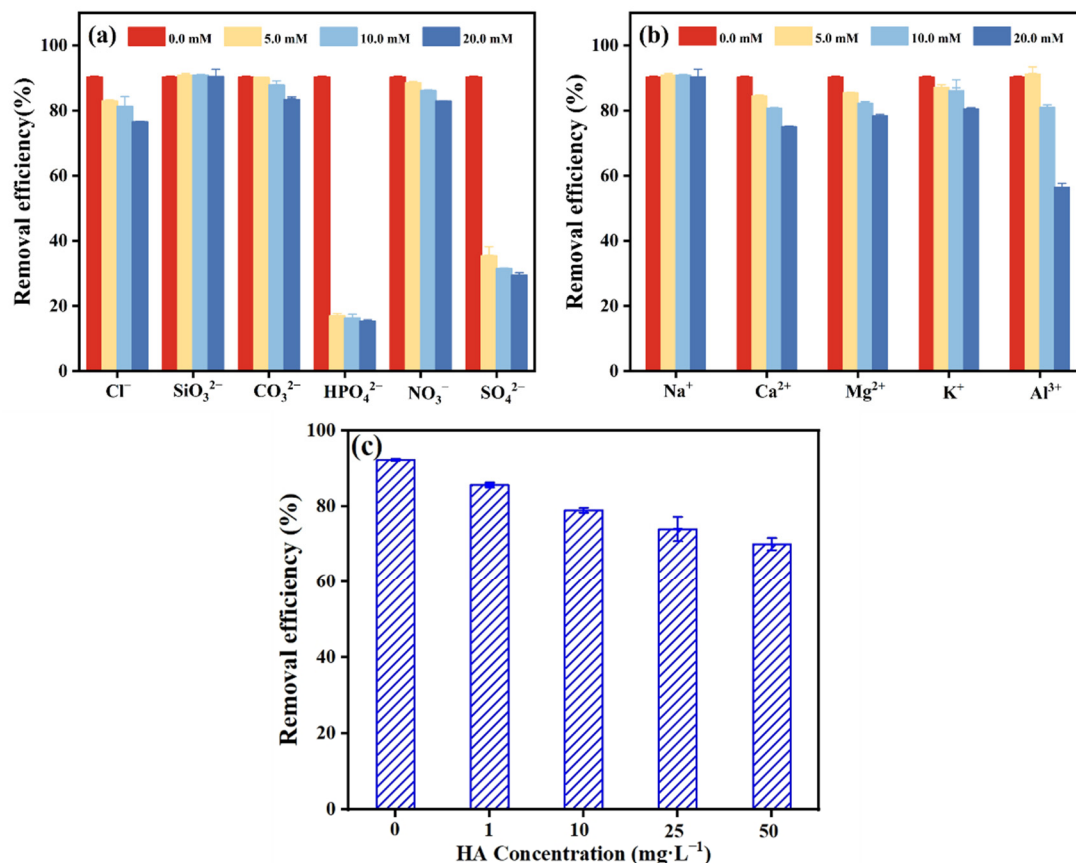


**Figure 5.** Effect of (a,b) common anions, cations, and (c) humic acid on the adsorption of Sb(V) by PB (experimental conditions:  $[Sb(V)]_0 = 10 \text{ mg}\cdot\text{L}^{-1}$ ; [anion and cation] = 5.0–20.0 mM; [HA] = 1–50  $\text{mg}\cdot\text{L}^{-1}$ ,  $\text{pH}_{\text{initial}} = 5.0$ ; temperature of 298 K). Data shown are the means and standard deviations of triplicated experiments.

### 3.6. Removal Mechanisms of Sb(V) by PB

Upon analyzing the spectra of the PB material before and after the sorption, the potential mechanism for the removal of Sb(V) was further examined using FTIR and XPS.

As presented in Figure 6, after the adsorption of Sb(V), the intensity of the O-H peaks at  $3422 \text{ cm}^{-1}$  and  $2093 \text{ cm}^{-1}$  decreased, but the peaks corresponding to  $Sb(OH)_6^{-1}$  appeared at  $3297 \text{ cm}^{-1}$  and  $2050 \text{ cm}^{-1}$ , indicating that O-H was involved in the complexation of Sb(V) [39]. Upon adsorption of Sb(V), there was a significant decrease in the peak intensity of both the H-O-H vibration peak at  $1632 \text{ cm}^{-1}$  and the Al-O-H peak at  $1072 \text{ cm}^{-1}$ . This indicated that the Al-O-H participated in the removal of Sb(V) by forming complexations (Al-O-Sb). Moreover, because the pH value affects the protonation state of functional groups, the main form of the Al-O-H group under acidic conditions was the protonation form, which adsorbed negative ions  $[Sb(OH)_6]^{-}$  by electrostatic attraction [9]. The Al-O peak at  $499 \text{ cm}^{-1}$  caused a significant increase in the shoulder peak after Sb(V) adsorption, which might be because the Al-O bond was not involved in the synthesis of new compounds. Similarly, numerous hydroxyl groups on the surface of PB had the potential to act as hydrogen donors and created hydrogen bonds with the oxygen atoms on Sb(V) molecules [42].

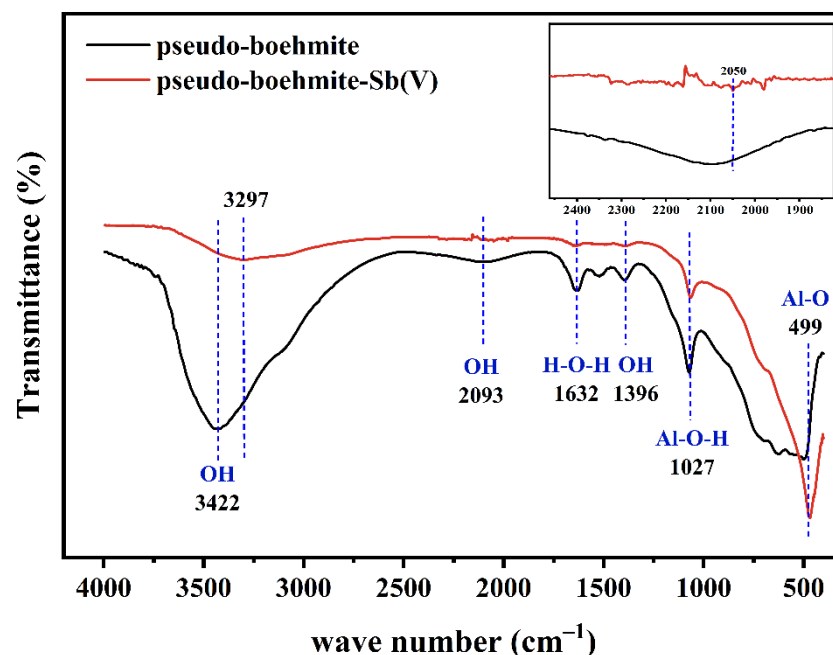


**Figure 6.** FTIR spectra of PB before and after Sb(V) adsorption.

The adsorption process of Sb(V) by PB was further explained through XPS survey scanning and narrow scan analysis of the elements on the surface of the PB before and after Sb(V) adsorption. As depicted in Figure 7a, the broad XPS spectrum of unreacted PB reveals the presence of Al and O, confirming the purity of the adsorbent. After reacting with Sb(V), spectroscopic measurements revealed the presence of antimony adsorption peaks, confirming the adsorption of Sb(V) on PB. After PB adsorption, the element content of Al peak decreased from 29.73% to 26.98%, and the binding energy increased from 74.20 eV to 74.62 eV, which confirmed the formation of the Al-O-Sb inner-sphere complex. At the same time, the Sb element content rose by 2.40%, suggesting the successful adsorption and stabilization of Sb within the internal structure of PB. The increase in oxygen (O) content from 70.27% to 70.62% was due to the overlap between the O 1s spectrum and the Sb 3d<sub>5/2</sub> spectrum, and the adsorbed 531 eV peak belonged to it. In the narrow scan spectrum of O 1s + Sb 3d (Figure 7e), the Sb 3d<sub>3/2</sub> peak emerged, indicating the chemical bonding of Sb with PB [43,44]. These findings substantiated that Sb(V) was chemically bound to the surface of PB after being absorbed in the solution. Based on the above analyses, the potential mechanisms were depicted in Figure 8, and the potential adsorption mechanism of Sb(V) on PB might be stated as follows:

- (1) The adsorption kinetic of Sb(V) on PB conformed to the pseudo-second-order model, indicating that the adsorption of Sb(V) was chemisorption. The isothermal model studies demonstrated that Sb(V) adsorption was a homogeneous monolayer and multilayer chemisorption process.
- (2) The influence of pH experiments showed that electrostatic attraction was involved in the process of Sb(V) removal by PB.
- (3) FTIR and XPS analyses revealed that Sb(V) was adsorbed by surface complexation (Al-O-Sb) and hydrogen bonding.

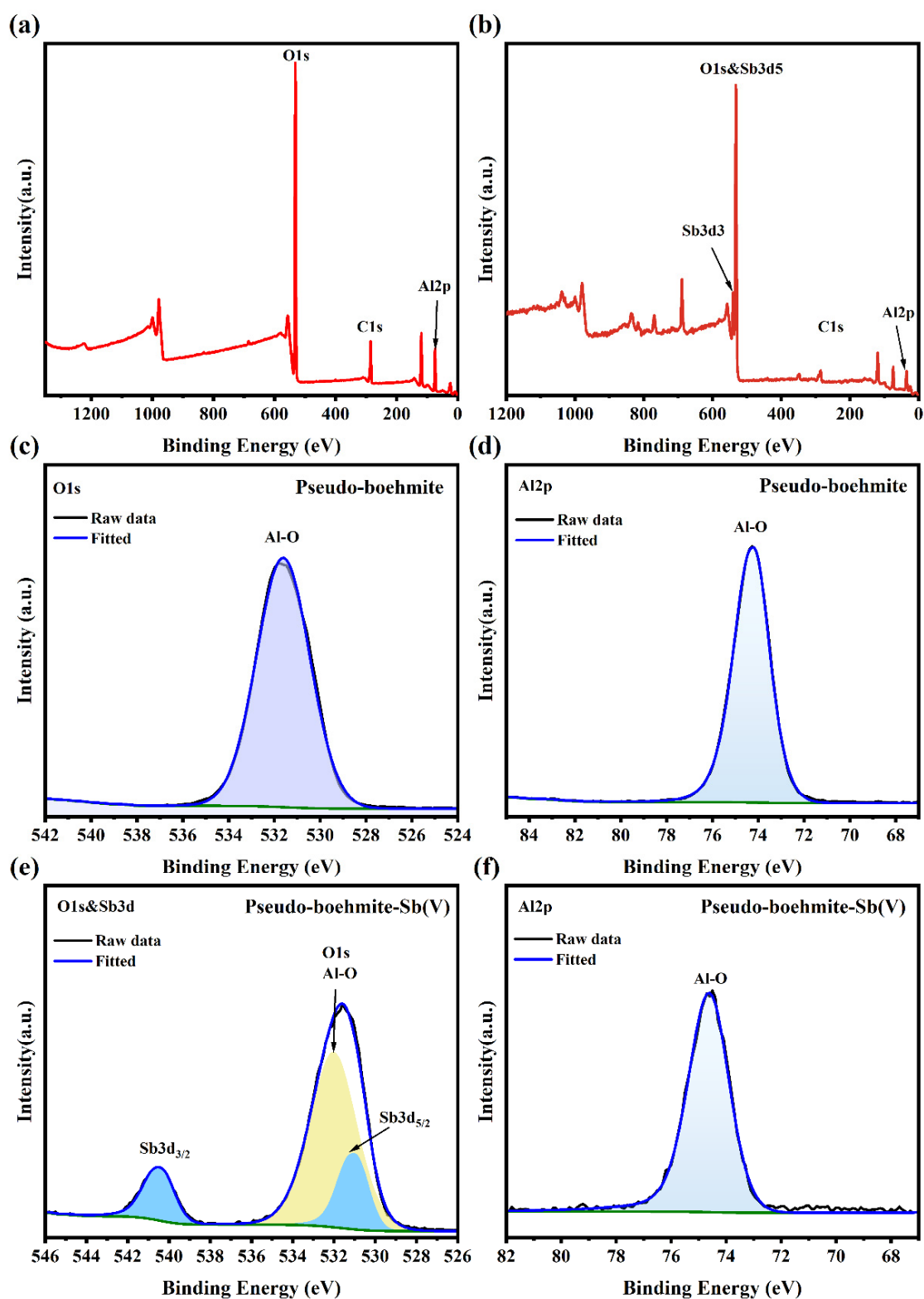


**Figure 7.** (a,b) Full-range XPS spectra of PB before Sb(V) adsorption and after Sb(V) adsorption; (c,d) O 1s and Al 2p spectra of PB before Sb(V) adsorption; (e,f) O 1s and Sb 3d and Al 2p spectra of PB after Sb(V) adsorption.

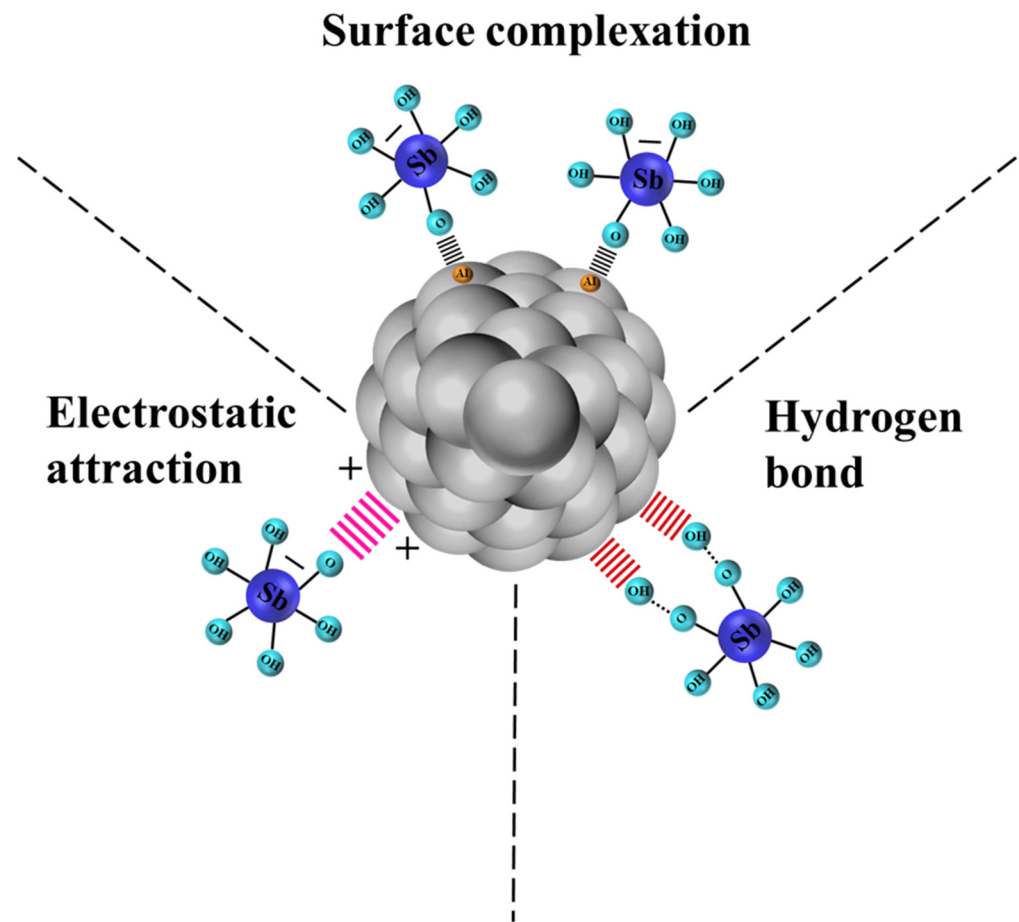


**Figure 8.** Removal mechanisms of Sb(V) by PB.

### 3.7. Reusability of PB for Sb(V)

Evaluating the reusability of adsorbents can offer a more comprehensive understanding of their performance in practical wastewater treatment applications. As shown in Figure 9, the analysis results implied that 82.82% and 78.23% of Sb(V) were removed by  $1.0 \times 10^{-4}$  M NaOH and DW desorption after the fifth cycle, respectively. Some materials, such as chitosan, use 0.1 M hydrochloric acid as the desorption agent [45]. However, hydrochloric acid is regulated in China, which may pose problems for desorption processes. Other materials like biochar and nanoparticles are desorbed using 0.5 M NaOH solution [6,9], while the concentration of desorption agent needed for PB is lower. These results indicate that the desorption of PB is more economical and convenient compared to other adsorbents. Additionally, some methods such as immobilizing PB onto a solid support or substrate or incorporating magnetic nanoparticles into the PB structure can ensure the sustainable use of PB in water treatment applications.

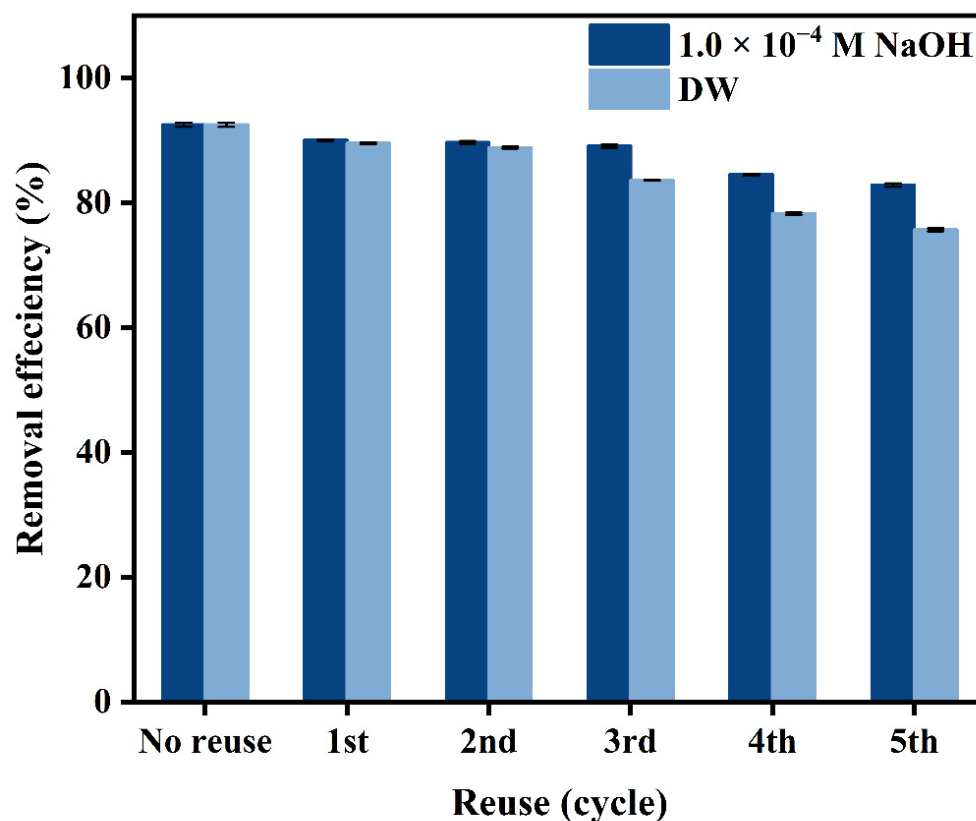


Figure 9. Reusability of PB for removal of Sb(V).

#### 4. Conclusions

In this research, PB was synthesized via aluminum alcohol hydrolysis. Compared to the high-temperature calcination required for the preparation of other materials such as biochar, the energy consumed during PB preparation is lower. The Sb(V) removal efficiency of PB was examined through batch experiments, and its characteristics were analyzed before and after adsorption. The experimental results fitted better with the pseudo-second-order model, Langmuir model, and Freundlich model, indicating the adsorption of Sb(V) by PB was a homogeneous monolayer and multilayer chemisorption process. Moreover, the adsorption mechanisms were determined to be surface complexation, electrostatic attraction, and hydrogen bonding. The complexation of hydroxyl groups with Sb(V) constituted a crucial adsorption mechanism for enhancing the removal efficiency of Sb(V). In conclusion, PB is a promising candidate for the remediation of wastewater pollution.

**Supplementary Materials:** The following supporting information can be downloaded at: <https://www.mdpi.com/article/10.3390/w16081172/s1>, Figure S1: Effect of dosage on Sb(V) removal by the PB; Figure S2: Leaching of aluminium ions during PB adsorption of Sb(V); Table S1: The abbreviation list.

**Author Contributions:** Y.H.: Conceptualization, Methodology, Investigation, Writing—original draft. Q.M.: Supervision, Methodology, Investigation, Writing—review and editing. Y.Z.: Writing—review and editing. X.X.: Supervision, Investigation. L.L.: Supervision, Writing—review and editing, Funding acquisition. All authors have read and agreed to the published version of the manuscript.

**Funding:** This work was supported in parts by the Natural Science Foundation of China (Grant Nos. 42077380 and U20A2086), Hunan Provincial Key R&D (2019SK2281), the Science and Technology Innovation Program of Hunan Province (2021GK4056), and the Ecological & Environmental Research Project of Hunan Province (HBKYXM-2023016).

**Data Availability Statement:** The data presented in this study are available on request from the corresponding author. The data are not publicly available due to commercial restrictions.

**Conflicts of Interest:** The authors declare that they have no known competing financial interests or personal relationships that could have appeared to influence the work reported in this paper.

## References

1. Lan, B.; Wang, Y.; Wang, X.; Zhou, X.; Kang, Y.; Li, L. Aqueous arsenic (As) and antimony (Sb) removal by potassium ferrate. *Chem. Eng. J.* **2016**, *292*, 389–397. [[CrossRef](#)]
2. Wu, T.-L.; Sun, Q.; Fang, G.-D.; Cui, P.-X.; Liu, C.; Alves, M.E.; Qin, W.-X.; Zhou, D.-M.; Shi, Z.-Q.; Wang, Y.-J. Unraveling the effects of gallic acid on Sb(III) adsorption and oxidation on goethite. *Chem. Eng. J.* **2019**, *369*, 414–421. [[CrossRef](#)]
3. Zeldin, J.; Tran, T.T.; Yadav, M.; Chaudhary, P.P.; D'Souza, B.N.; Ratley, G.; Ganesan, S.; Myles, I.A. Antimony Compounds Associate with Atopic Dermatitis and Influence Models of Itch and Dysbiosis. *Environ. Sci. Technol. Lett.* **2023**, *10*, 452–457. [[CrossRef](#)] [[PubMed](#)]
4. Wang, X.; He, M.; Xi, J.; Lu, X. Antimony distribution and mobility in rivers around the world's largest antimony mine of Xikuangshan, Hunan Province, China. *Microchem. J.* **2011**, *97*, 4–11. [[CrossRef](#)]
5. Li, Q.; Ma, X.; Qi, C.; Li, R.; Zhang, W.; Li, J.; Shen, J.; Sun, X. Facile preparation of novel magnetic mesoporous Fe Mn binary oxides from Mn encapsulated carboxymethyl cellulose-Fe(III) hydrogel for antimony removal from water. *Sci. Total Environ.* **2022**, *821*, 153529. [[CrossRef](#)]
6. Guo, W.; Fu, Z.; Zhang, Z.; Wang, H.; Liu, S.; Feng, W.; Zhao, X.; Giesy, J.P. Synthesis of Fe<sub>3</sub>O<sub>4</sub> magnetic nanoparticles coated with cationic surfactants and their applications in Sb(V) removal from water. *Sci. Total Environ.* **2020**, *710*, 136302. [[CrossRef](#)] [[PubMed](#)]
7. Long, X.; Wang, X.; Guo, X.; He, M. A review of removal technology for antimony in aqueous solution. *J. Environ. Sci.* **2020**, *90*, 189–204. [[CrossRef](#)]
8. Salari, K.; Hashemian, S.; Baei, M.T. Sb (V) removal from copper electrorefining electrolyte: Comparative study by different sorbents. *Trans. Nonferrous Met. Soc. China* **2017**, *27*, 440–449. [[CrossRef](#)]
9. Wang, L.; Wang, J.; Wang, Z.; He, C.; Lyu, W.; Yan, W.; Yang, L. Enhanced antimonate (Sb(V)) removal from aqueous solution by La-doped magnetic biochars. *Chem. Eng. J.* **2018**, *354*, 623–632. [[CrossRef](#)]
10. Amen, R.; Bashir, H.; Bibi, I.; Shaheen, S.M.; Niazi, N.K.; Shahid, M.; Hussain, M.M.; Antoniadis, V.; Shakoob, M.B.; Al-Solaimani, S.G. A critical review on arsenic removal from water using biochar-based sorbents: The significance of modification and redox reactions. *Chem. Eng. J.* **2020**, *396*, 125195. [[CrossRef](#)]
11. Inam, M.A.; Khan, R.; Akram, M.; Khan, S.; Yeom, I.T. Effect of Water Chemistry on Antimony Removal by Chemical Coagulation: Implications of zeta-Potential and Size of Precipitates. *Int. J. Mol. Sci.* **2019**, *20*, 2945. [[CrossRef](#)] [[PubMed](#)]
12. Wang, L.; Luo, Y.; Li, H.; Yu, D.; Wang, Y.; Wang, W.; Wu, M. Preparation and selective adsorption of surface-imprinted microspheres based on hyperbranched polyamide-functionalized sodium alginate for the removal of Sb(III). *Colloids Surf. A Physicochem. Eng. Asp.* **2020**, *585*, 124106. [[CrossRef](#)]
13. Du, X.; Qu, F.; Liang, H.; Li, K.; Yu, H.; Bai, L.; Li, G. Removal of antimony (III) from polluted surface water using a hybrid coagulation-flocculation-ultrafiltration (CF-UF) process. *Chem. Eng. J.* **2014**, *254*, 293–301. [[CrossRef](#)]
14. Awual, M.R.; Alharthi, N.H.; Okamoto, Y.; Karim, M.R.; Halim, M.E.; Hasan, M.M.; Rahman, M.M.; Islam, M.M.; Khaleque, M.A.; Sheikh, M.C. Ligand field effect for Dysprosium(III) and Lutetium(III) adsorption and EXAFS coordination with novel composite nanomaterials. *Chem. Eng. J.* **2017**, *320*, 427–435. [[CrossRef](#)]
15. Wei, D.; Li, B.; Luo, L.; Zheng, Y.; Huang, L.; Zhang, J.; Yang, Y.; Huang, H. Simultaneous adsorption and oxidation of antimonite onto nano zero-valent iron sludge-based biochar: Indispensable role of reactive oxygen species and redox-active moieties. *J. Hazard. Mater.* **2020**, *391*, 122057. [[CrossRef](#)] [[PubMed](#)]
16. Zhao, T.; Tang, Z.; Zhao, X.; Zhang, H.; Wang, J.; Wu, F.; Giesy, J.P.; Shi, J. Efficient removal of both antimonite (Sb(III)) and antimonate (Sb(V)) from environmental water using titanate nanotubes and nanoparticles. *Environ. Sci. Nano* **2019**, *6*, 834–850. [[CrossRef](#)]
17. Zhang, Y.; Jiang, D.; Wang, Y.; Zhang, T.C.; Xiang, G.; Zhang, Y.-X.; Yuan, S. Core-Shell Structured Magnetic  $\gamma$ -Fe<sub>2</sub>O<sub>3</sub>@PANI Nanocomposites for Enhanced As(V) Adsorption. *Ind. Eng. Chem. Res.* **2020**, *59*, 7554–7563. [[CrossRef](#)]
18. Bai, Y.; Wu, F.; Gong, Y. Oxidation and adsorption of antimony (III) from surface water using novel Al<sub>2</sub>O<sub>3</sub>-supported Fe-Mn binary oxide nanoparticles: Effectiveness, dynamic quantitative mechanisms, and life cycle analysis. *Environ. Sci. Nano* **2020**, *7*, 3047–3061. [[CrossRef](#)]
19. Ramadugu, S.K.; Mason, S.E. DFT Study of Antimony(V) Oxyanion Adsorption on  $\alpha$ -Al<sub>2</sub>O<sub>3</sub>(1 $\bar{1}$ 0 $\bar{2}$ ). *J. Phys. Chem. C* **2015**, *119*, 18149–18159. [[CrossRef](#)]
20. Zhou, W.; Zhou, A.; Wen, B.; Liu, P.; Zhu, Z.; Finckrock, Z.; Zhou, J. Antimony isotope fractionation during adsorption on aluminum oxides. *J. Hazard. Mater.* **2022**, *429*, 128317. [[CrossRef](#)]
21. Zhang, M.; Gao, B. Removal of arsenic, methylene blue, and phosphate by biochar/AlOOH nanocomposite. *Chem. Eng. J.* **2013**, *226*, 286–292. [[CrossRef](#)]
22. Islam, M.A.; Angove, M.J.; Morton, D.W.; Pramanik, B.K.; Awual, M.R. A mechanistic approach of chromium (VI) adsorption onto manganese oxides and boehmite. *J. Environ. Chem. Eng.* **2020**, *8*, 103515. [[CrossRef](#)]
23. Chen, X.; Guan, X.; Zhang, H.; Liu, W.; Han, Y.; Xiong, J.; Zheng, S.; Zhang, Y.; Zhang, X.; Zhao, J.; et al. Green desorption combined with peptization technology for disposing of Cr(VI)-V(V)-containing hazardous aluminum waste to prepare high-valued pseudo-boehmite. *Sep. Purif. Technol.* **2023**, *314*, 123655. [[CrossRef](#)]

24. Cao, P.; Gao, D.; Luo, J.; Li, X.; Xing, L.; Jiang, H.; Li, G. Preparation of pseudo-boehmite via carbonation of sodium aluminate lixivium extracted from coal fly ash. *Microporous Mesoporous Mater.* **2024**, *366*, 112933. [[CrossRef](#)]
25. Xie, X.; Li, J.; Liu, J.; Chen, Z.; Yuan, X.; Chen, T.; Luo, L. Efficient degradation of chromium picolinate with simultaneous chromium removal from aqueous solutions using the Fenton process. *Sep. Purif. Technol.* **2023**, *317*, 123864. [[CrossRef](#)]
26. Panda, A.P.; Jha, U.; Swain, S.K. Synthesis of nanostructured copper oxide loaded boehmite (CuO\_Boehmite) for adsorptive removal of As(III/V) from aqueous solution. *J. Water Process Eng.* **2020**, *37*, 101506. [[CrossRef](#)]
27. Aljeboree, A.M.; Alshirifi, A.N.; Alkaim, A.F. Kinetics and equilibrium study for the adsorption of textile dyes on coconut shell activated carbon. *Arab. J. Chem.* **2017**, *10*, S3381–S3393. [[CrossRef](#)]
28. Mishra, S.; Dwivedi, J.; Kumar, A.; Sankararamkrishnan, N. Removal of antimonite (Sb(III)) and antimonate (Sb(V)) using zerovalent iron decorated functionalized carbon nanotubes. *RSC Adv.* **2016**, *6*, 95865–95878. [[CrossRef](#)]
29. Wang, Z.; Gong, J.; Ma, J.; Xu, J. In situ growth of hierarchical boehmite on 2024 aluminum alloy surface as superhydrophobic materials. *RSC Adv.* **2014**, *4*, 14708–14714. [[CrossRef](#)]
30. Chen, Y.; Cai, W.; Dang, C.; Fan, J.; Zhou, J.; Liu, Z. A facile sol–gel synthesis of chitosan–boehmite film with excellent acid resistance and adsorption performance for Pb(II). *Chem. Eng. Res. Des.* **2020**, *161*, 332–339. [[CrossRef](#)]
31. Cai, W.; Li, H.; Zhang, Y. Influences of processing techniques of the H<sub>2</sub>O<sub>2</sub>-precipitated pseudoboehmite on the structural and textural properties of  $\gamma$ -Al<sub>2</sub>O<sub>3</sub>. *Colloids Surf. A Physicochem. Eng. Asp.* **2007**, *295*, 185–192. [[CrossRef](#)]
32. Panda, A.P.; Giri, M.; Jena, K.K.; Alhassan, S.M.; Kumar, S.A.; Jha, U.; Swain, S.K. Understanding the As(III) oxidative performance of MnO<sub>2</sub> polymorphs ( $\alpha$ ,  $\beta$ , and  $\gamma$ ) and synthesis of an efficient nanocomposite of iron ore slime derived 2-line ferrihydrite and  $\gamma$ -MnO<sub>2</sub> for sequestration of total arsenic from aqueous solution. *Chem. Eng. J.* **2022**, *442*, 136075. [[CrossRef](#)]
33. Kang, D.; Yu, X.; Ge, M.; Lin, M.; Yang, X.; Jing, Y. Insights into adsorption mechanism for fluoride on cactus-like amorphous alumina oxide microspheres. *Chem. Eng. J.* **2018**, *345*, 252–259. [[CrossRef](#)]
34. Guo, X.; Wu, Z.; He, M.; Meng, X.; Jin, X.; Qiu, N.; Zhang, J. Adsorption of antimony onto iron oxyhydroxides: Adsorption behavior and surface structure. *J. Hazard. Mater.* **2014**, *276*, 339–345. [[CrossRef](#)]
35. Wang, H.; Lv, Z.; Wang, B.; Wang, Y.-N.; Sun, Y.; Tsang, Y.F.; Zhao, J.; Zhan, M. Effective stabilization of antimony in Waste-to-Energy fly ash with recycled laboratory iron-rich residuals. *J. Clean. Prod.* **2019**, *230*, 685–693. [[CrossRef](#)]
36. Liu, Y.; Meng, L.; Han, K.; Sun, S. Synthesis of nano-zirconium-iron oxide supported by activated carbon composite for the removal of Sb(V) in aqueous solution. *RSC Adv.* **2021**, *11*, 31131–31141. [[CrossRef](#)] [[PubMed](#)]
37. Qi, Z.; Joshi, T.P.; Liu, R.; Liu, H.; Qu, J. Synthesis of Ce(III)-doped Fe<sub>3</sub>O<sub>4</sub> magnetic particles for efficient removal of antimony from aqueous solution. *J. Hazard. Mater.* **2017**, *329*, 193–204. [[CrossRef](#)] [[PubMed](#)]
38. Robati, D.; Rajabi, M.; Moradi, O.; Najafi, F.; Tyagi, I.; Agarwal, S.; Gupta, V.K. Kinetics and thermodynamics of malachite green dye adsorption from aqueous solutions on graphene oxide and reduced graphene oxide. *J. Mol. Liq.* **2016**, *214*, 259–263. [[CrossRef](#)]
39. Li, L.; Liao, L.; Wang, B.; Li, W.; Liu, T.; Wu, P.; Xu, Q.; Liu, S. Effective Sb(V) removal from aqueous solution using phosphogypsum-modified biochar. *Environ. Pollut.* **2022**, *301*, 119032. [[CrossRef](#)]
40. Chen, H.; Gao, Y.; El-Naggar, A.; Niazi, N.K.; Sun, C.; Shaheen, S.M.; Hou, D.; Yang, X.; Tang, Z.; Liu, Z.; et al. Enhanced sorption of trivalent antimony by chitosan-loaded biochar in aqueous solutions: Characterization, performance and mechanisms. *J. Hazard. Mater.* **2022**, *425*, 127971. [[CrossRef](#)]
41. Li, X.; Dou, X.; Li, J. Antimony(V) removal from water by iron-zirconium bimetal oxide: Performance and mechanism. *J. Environ. Sci.* **2012**, *24*, 1197–1203. [[CrossRef](#)] [[PubMed](#)]
42. Wang, F.; Sun, H.; Ren, X.; Zhang, K. Sorption of naphthalene and its hydroxyl substitutes onto biochars in single-solute and bi-solute systems with propranolol as the co-solute. *Chem. Eng. J.* **2017**, *326*, 281–291. [[CrossRef](#)]
43. Chen, L.; Cui, W.; Li, J.; Wang, H.; Chen, P.; Zhou, Y.; Dong, F. The high selectivity for benzoic acid formation on Ca<sub>2</sub>Sb<sub>2</sub>O<sub>7</sub> enables efficient and stable toluene mineralization. *Appl. Catal. B Environ.* **2020**, *271*, 118948. [[CrossRef](#)]
44. Guo, W.; Fu, Z.; Wang, H.; Liu, S.; Wu, F.; Giesy, J.P. Removal of antimonate (Sb(V)) and antimonite (Sb(III)) from aqueous solutions by coagulation-flocculation-sedimentation (CFS): Dependence on influencing factors and insights into removal mechanisms. *Sci. Total Environ.* **2018**, *644*, 1277–1285. [[CrossRef](#)]
45. Xiong, N.; Wan, P.; Zhu, G.; Xie, F.; Xu, S.; Zhu, C.; Hursthouse, A.S. Sb(III) removal from aqueous solution by a novel nano-modified chitosan (NMCS). *Sep. Purif. Technol.* **2020**, *236*, 116266. [[CrossRef](#)]

**Disclaimer/Publisher’s Note:** The statements, opinions and data contained in all publications are solely those of the individual author(s) and contributor(s) and not of MDPI and/or the editor(s). MDPI and/or the editor(s) disclaim responsibility for any injury to people or property resulting from any ideas, methods, instructions or products referred to in the content.